

# Optimization design of process parameters for cold and hot composite roll forming of the AHSS square tube using response surface methodology

Yu Wang

Zelalem Abathun Mehari

Junyuan Wu

Jingtao Han (✉ [hanjt@ustb.edu.cn](mailto:hanjt@ustb.edu.cn))

University of Science and Technology Beijing

---

## Research Article

**Keywords:** AHSS, Cold and hot composite roll forming, Corner radius, Microcrack, Response surface methodology, Optimization

**Posted Date:** April 11th, 2022

**DOI:** <https://doi.org/10.21203/rs.3.rs-1522445/v1>

**License:** © ⓘ This work is licensed under a Creative Commons Attribution 4.0 International License.

[Read Full License](#)

---

# **Optimization design of process parameters for cold and hot composite roll forming of the AHSS square tube using response surface methodology**

Yu Wang<sup>1</sup>, Zelalem Abathun Mehari<sup>1</sup>, Junyuan Wu<sup>2</sup>, Jingtao Han<sup>1,3\*</sup>

<sup>1</sup>School of Materials Science and Engineering, University of Science and Technology Beijing, Beijing 100083, China

<sup>2</sup>Technique Center of Guangxi Liuzhou Iron and Steel Group Co. Ltd., Liuzhou 545002, China

<sup>3</sup>Sino Institute of Roll Forming Industry (Caofeidian) Co. Ltd., Tangshan 063200, China

E-mail: hanjt@ustb.edu.cn

## **Abstract**

Advanced high-strength steel (AHSS) is a highly competitive material for the automobile industry to resolve the challenge of weight reduction and passenger safety. With the increase in strength, defects such as microcrack, local thickness reduction, and large corner radius in the corner section of cold roll-formed steel products become more and more serious. Cold and hot composite roll forming (CHCRF) is a newly developed manufacturing technology that combines the advantages of cold and hot forming to overcome the challenge of forming AHSS. In this paper, the mathematical models that represent the effect of line velocity, heating power, and deformation amount on the yield strength, outer corner radius, and microcrack length of the corner section of cold and hot composite roll-formed AHSS square tube are investigated by the response surface methodology (RSM) with Box-Behnken design (BBD). From the analysis of variance (ANOVA), it is found that all the three process parameters play a significant role in the outer corner radius and microcrack length, while the line velocity and heating power influence the yield strength

significantly. Furthermore, an optimization process is proposed, with the outer corner radius and microcrack length as objective functions and the yield strength as a constrained condition, to manufacture the AHSS square tube with a small outer corner radius and no microcrack defect. Experimental verification has been conducted using the optimal process parameters, and the average magnitude of error is about 5 %, which implies that the optimization design is accurate and reliable.

**Keywords:** AHSS, Cold and hot composite roll forming, Corner radius, Microcrack, Response surface methodology, Optimization

## **1 Introduction**

With the development of the automobile industry, fuel consumption, air pollution, and passenger safety are becoming more and more important. The application of advanced high-strength steel (AHSS) in automotive structural components is an efficient way to advance automotive lightweight technology, which can simultaneously achieve energy conservation, emission reduction, and safety performance improvement [1–3].

Cold roll forming (CRF) is a process of making uniform cross-section products from sheet, strip, or coiled stock by feeding the strips through successive pairs of rolls arranged in tandem [4]. CRF is characterized by high production efficiency, good surface quality, and low cost, which has become one of the most common forming processes for AHSS products. However, due to the poor ductility of AHSS, lots of product defects such as microcrack [5, 6], springback [7, 8], thickness reduction [9], large corner radius [10, 11] and residual stress [12, 13] are more likely to occur during the forming process. In addition, the requirements for the equipment are also higher [14].

To improve the quality of AHSS products, many scholars have focused on the forming mechanism of defects and the optimization of process parameters. Moneke et al. [15] investigated the creation of end flare during the CRF and presented a countermeasure to reduce end flare by adopting the roll gap [16]. Cheng et al. [17] developed the UDT (USTB-Durable T) -type angle adjusting method to compensate springback with the improvement of the edge waves and asymmetric behavior. Su et al. [18] proposed a five-boundary conditional distribution function of the forming angle to decrease stress, strain, and springback at each forming stand. Abeyrathna et al. [19] presented a first step towards an in-line shape compensation method to estimate shape defects and the subsequent re-adjustment of tooling for compensation. Tajik et al. [20] presented the asymmetrical forming rolls to achieve more symmetrical flanges and smaller twist defects in the CRF of asymmetrical-channel sections. Shirani et al. [21] found that the most important parameters to the bowing defect of CRF products are the bending angle increment at each stand, the flange width, and strip thickness.

On the other hand, some scholars have developed advanced sheet metal forming processes based on the CRF to achieve new product features. Due to the CRF being limited to the production of profiles with constant cross-sections in the longitudinal direction, Groche et al. [22] introduced the flexible roll forming (FRF) process to manufacture profiles with variable cross-sections by controlling the roll stands with CNC. Yan et al. [23] established a finite element model of a six passes FRF process and verified the numerical result with the experiment of a B pillar reinforcing plate made of AHSS. Similarly, Park et al. [24] proposed a new process called incremental counter forming (ICF) to reduce the shape error of the FRF process. Ding et al. [25] proposed millipede forming to overcome fundamental limitations in the CRF. Chain-die forming is also a promising novel sheet metal forming method, which can significantly decrease or even eliminate the

redundant plastic deformations occurring in the CRF [26]. Li et al. [27] investigated the performance of AHSS in chain-die forming by experiment and simulation.

As mentioned above, adopting more reasonable process parameters or applying a new forming process based on the CRF can effectively improve a range of defects or achieve new product features, but there are still three unresolved problems, which will get worse as the material strength increases. The first one is the strain hardening effect, the second one is the thickness reduction, and the third one is the minimum bending radius. Basically, the first two problems, which are caused by dislocation tangle and neutral layer inside displacement are common characteristics in the bend zone. The last problem is that the higher the material strength, the greater the minimum bending radius, which is otherwise prone to microcrack defects. The corner section of a cold roll-formed AHSS square tube is usually characterized by the high yield strength, thickness reduction, and large outer corner radius. Too high yield strength will lead to brittle failure easily while the thickness reduction will degrade the safety performance of the tube seriously. The square tube is preferred in the industrial field due to the square section can be joined at any angle by welding compared to the circular tube, which means the larger the outer corner radius, the harder the assembly and welding process.

The introduction of heating technology into the roll forming process can increase the ductility of AHSS greatly to avoid defects in the subsequent forming process. Lindgren et al. [28] used a prototype resistance heating machine to make the partial heating experiments, finding that the partially heated materials could be roll-formed to  $120^\circ$  without rupture while the unheated material could be roll-formed to  $30^\circ$  but ruptured in the bending zone at  $60^\circ$ . Kim et al. [29] introduced a pre-heating using a gas torch and found that springback, bow, and buckling with the

roll forming process involving pre-heating got improved by  $0.97^\circ$ , 0.17 mm, and 0.20, respectively, compared to the same CRF processes.

In order to solve the above-mentioned three problems, this study puts forward an advanced manufacturing process called cold and hot composite roll forming (CHCRF), using the hot roll forming (HRF) to reprocess the cold roll-formed product. As the most important part of CHCRF, HRF selects the local induction heating to preheat the region to be formed, which is safer, energy-efficient, environmentally friendly, and suitable for mass industrial production compared to other heating technologies. HRF can break the forming limit of CRF by increasing the ductility of steel materials. However, the previous investigation by Peng et al. [30] showed that the microcrack defect occurred during the HRF process of AHSS square tubes while only the influence of heating temperature was studied. Thus, it is necessary to consider the comprehensive influence of various process parameters and obtain the optimization design to improve product quality.

This paper presents an approach for optimization design of process parameters for CHCRF of AHSS square tube using RSM and establishes the experiment schedule based on Box-Behnken design (BBD), where three process parameters (heating power, line velocity, and deformation amount) have been proposed to analyze and predict yield strength, outer corner radius, and microcrack length of the corner section of AHSS square tube. The nonlinear relationship between the responses and process parameters is presented by mathematical models. According to the optimization evaluation criteria, the three process parameters are optimized and then the experimental verification is carried out under the optimal combination of the process parameters.

## 2 Methodologies

### 2.1 Process principle

CHCRF is a two-step forming technology that adopts CRF first and then HRF, and vice versa. In the case of the AHSS square tube, CRF is adopted to obtain the cold roll-formed tube first, subsequently, the HRF technology is adopted to improve the corner section performance and optimize the geometric structure to obtain the tube with sharp corners.

In general, there are two main CRF processes to produce square tubes, namely Flat-Strip-to-Square forming and Circle-to-Square forming [31]. The schematic representation of the two processes is shown in Fig. 1. The Flat-Strip-to-Square forming process requires fewer forming passes, but the corner section has more serious quality problems, such as uneven corner radius and thickness reduction. Although the Circle-to-Square forming process needs more forming passes, the corner radius is much more uniform and the corner thickness will increase slightly.

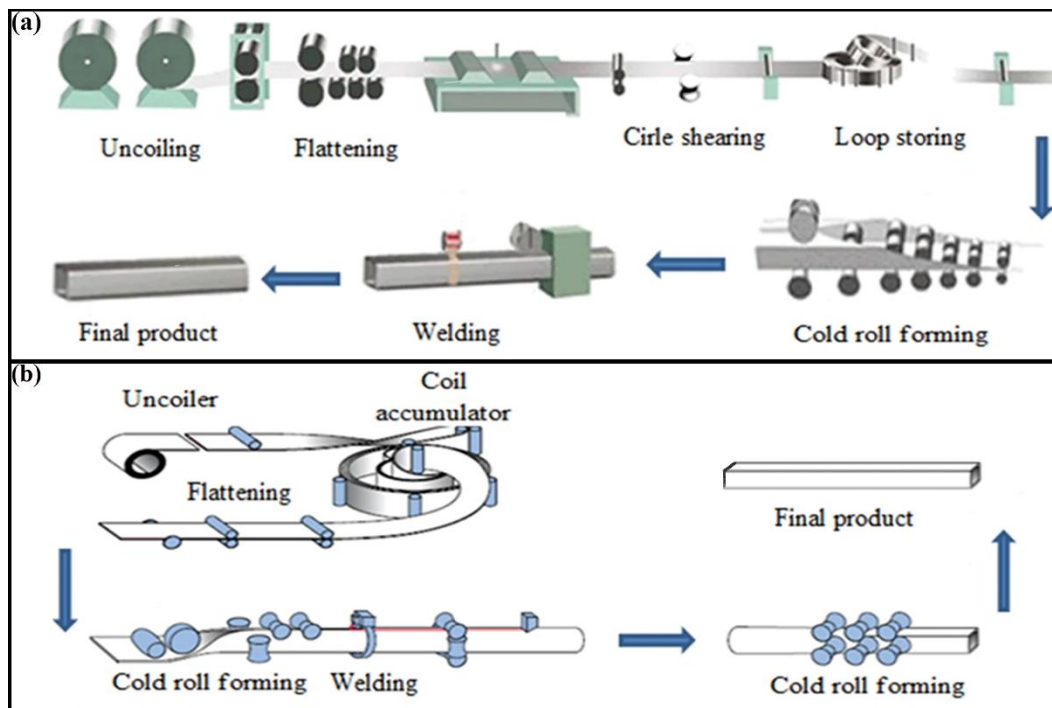


**Fig. 1** Schematic diagram of CRF processes for the square tube: (a) Flat-Strip-to-Square forming; (b) Circle-to-Square forming

The square tube made by the above two processes can be used as the raw material for HRF. As shown in Fig. 2, the HRF line consists of four forming stands, named Stand 1, Stand 2, Stand 3, and Stand 4. The basic idea of HRF is to heat the corner section of the square tube rapidly with an induction heating coil first, and then compress the straight section of the square tube with the top, side, and bottom rolls in Stand 2, Stand 3, and Stand 4. Because the temperature difference between the straight and corner sections has caused the ductility difference, plastic deformation will occur mainly in the corner section, which means the metal will flow from the straight section to the corner section to build sharper corners.

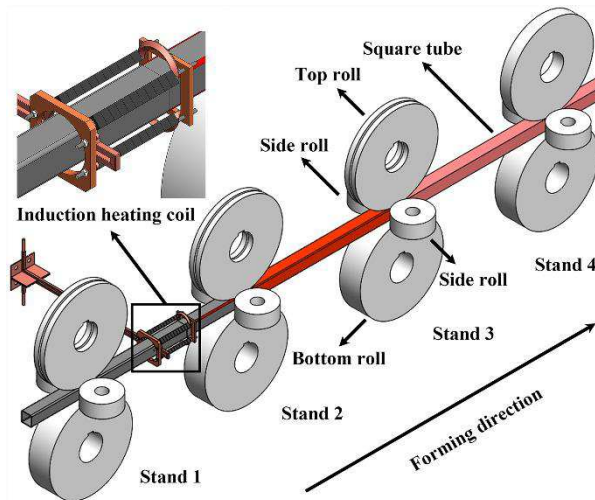


**Fig. 2** Schematic diagram of HRF for the square tube

## 2.2 Main process parameters

The main process parameters of HRF include heating power, line velocity, and deformation amount. The heating power, which can be adjusted by the control panel on the induction heating equipment, directly affects the heating speed and the range of induction heating. Bui et al. [32]

found that line velocity appears to play a minor role in CRF. However, the linear velocity becomes much more important in HRF, because it will determine the time required to pass the square tube through the heating coil, thus affecting the heating temperature distribution. Since the relational expression between linear velocity, roll diameter, and motor speed has been written into the control system, the linear velocity value can be entered directly on the touch screen. The deformation amount, which is used to describe the degree of plastic deformation during the HRF, is similar to the forming angle in CRF.

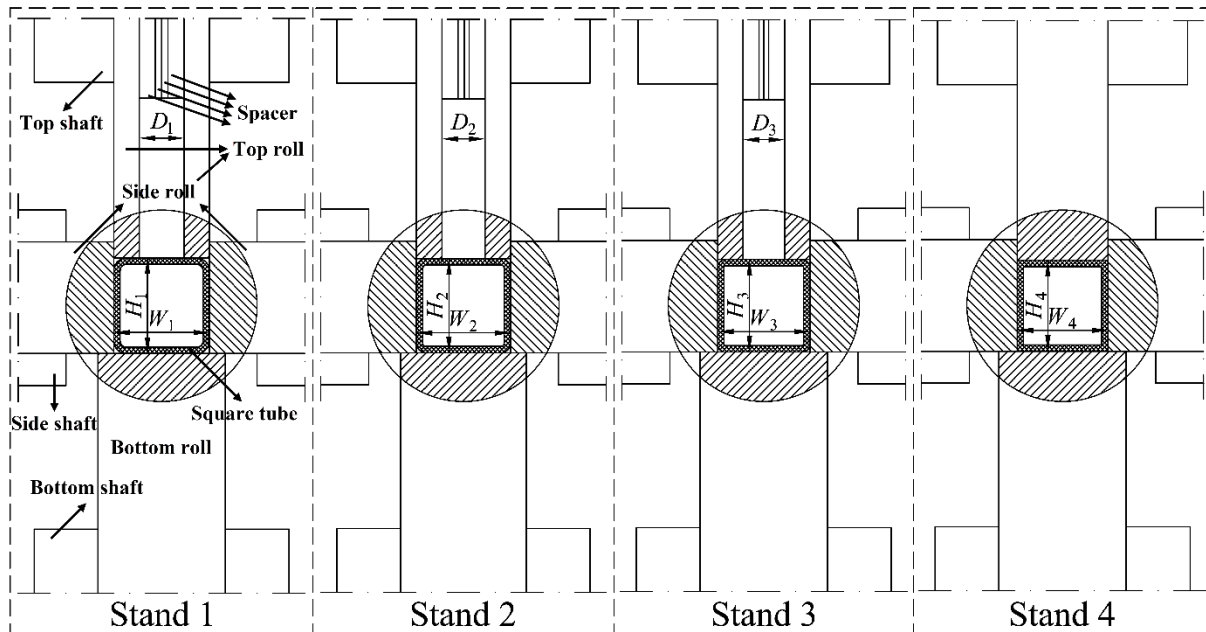


**Fig. 3** Schematic diagram of roll pass design

To apply the downhill strategy [33, 34], both the top and bottom shafts are adjustable in height, which means the center points of all roll passes are kept in a horizontal line. Since plastic deformation mainly occurs in the corner section, the top rolls of Stand 1, Stand 2, and Stand 3, as shown in Fig. 3, are split into two parts in the middle to change the horizontal dimension of the roll pass by replacing the half-round spacers instead of rolls. Finally, the top roll of Stand 4 will

contact the entire upper surface of the square tube to ensure good evenness between the straight and corner sections. The corresponding functions for the deformation amount and roll pass dimension can be expressed as follows:

$$W_1 = W, H_1 = H \quad (1)$$

$$W_1 - W_2 = D_1 - D_2 \quad (2)$$

$$W_2 - W_3 = D_2 - D_3 \quad (3)$$

$$A = W_1 - W_4 + H_1 - H_4 \quad (4)$$

where  $W$  and  $H$  are the width and height of the square tube, respectively,  $W_1$ ,  $W_2$ ,  $W_3$ , and  $W_4$  are the horizontal dimensions of roll pass in Stand 1, Stand 2, Stand 3, and Stand 4, respectively,  $D_1$ ,  $D_2$ , and  $D_3$  are the thicknesses of all the spacers in Stand 1, Stand 2, and Stand 3, respectively,  $H_1$  and  $H_4$  are the vertical dimensions of roll pass in Stand 1 and Stand 4, respectively,  $A$  is the deformation amount.

### 2.3 Design of experiments

Response surface methodology (RSM) is a collection of mathematical and statistical techniques that can be used to investigate the comprehensive relations between a series of independent design variables and the desired responses. The quadratic mathematical model for responses can be prescribed as follows:

$$y = F(x) = \beta_0 + \sum_{i=1}^n \beta_i x_i + \sum_{i=1}^n \beta_{ii} x_i^2 + \sum_{i=1, j>1}^n \beta_{ij} x_i x_j \quad (5)$$

where  $y$  is the response,  $x$  is the design variable,  $\beta_0$  is the constant term,  $\beta_i$  is the slope or linear effect of the design variable  $x_i$ ,  $\beta_{ii}$  is the quadratic effect of the design variable  $x_i$ ,  $\beta_{ij}$  is the

linear-by-linear interaction effect between the design variables  $x_i$  and  $x_j$ ,  $n$  is the number of design variables.

Since the main idea of RSM is to obtain the optimal response by using a sequence of designed experiments, there are several response surface design methods, such as central composite design (CCD) and Box–Behnken design (BBD). The BBD is more efficient to arrange and interpret experiments than other methods [35]. The BBD with three factors is applied in this study, and the levels are shown in Table 1.

**Table 1.** Levels of the design variables

Design variables	Coded value	Actual value	Levels		
			-1	0	1
Linear velocity $V$ / (m·min <sup>-1</sup> )	$x_1$	$X_1$	2	3	4
Heating power $P$ / (kW)	$x_2$	$X_2$	42.5	47.5	52.5
Deformation amount $A$ / (mm)	$x_3$	$X_3$	3	4	5

The relationships between the coded and actual values of the three design variables can be defined as follows:

$$x_1 = X_1 - 3, \quad x_2 = \frac{X_2 - 47.5}{5}, \quad x_3 = X_3 - 4 \quad (6)$$

where  $x_1$ ,  $x_2$ , and  $x_3$  are the coded values of linear velocity, heating power, and deformation amount, respectively,  $X_1$ ,  $X_2$ , and  $X_3$  are the actual values of linear velocity, heating power, and deformation amount, respectively.

### 3 Experimental work

#### 3.1 Experimental samples

The square tube samples material used in the experiment is QSTE700TM AHSS and its chemical composition is shown in Table 2. The number 700 indicates that the yield strength is not less than 700 MPa and this kind of AHSS square tube has been widely used in the bus body structure and automotive frame. The width, height, wall thickness, and outer corner radius of the square tube are about 40mm, 40mm, 2mm, and 4mm, respectively. Considering the HRF line has four forming stands and the stand distance is 600 mm, the length of every square tube sample is cut to 2000 mm.

**Table 2.** Chemical composition of QSTE700TM AHSS (mass fraction/ %)

C	N	Mn	Si	Cu	Ti	Nb	Mo	Cr	Al	P	S	Fe
0.08	0.0045	1.9	0.13	0.015	0.091	0.07	0.13	0.042	0.043	0.015	0.007	Bal.

#### 3.2 Experimental setup

The HRF line used in the experiment is shown in Fig. 4. The induction equipment is placed on an adjustable shelf to adjust the centerline of the induction coil and roll pass to be the same, otherwise, it will cause uneven heating in the corner section. Since the induction heating process is hard to observe closely, the security camera is used to monitor the heating area and transmit real-time images to the console screen. Meanwhile, the infrared temperature sensor is turned to point to the coil exit, measuring the heating temperature of the corner section. The roll pass design and arrangement are the same as in Fig. 3, the main innovation of which is the use of half-round spacers to avoid frequent replacement of top rolls. In order to ensure continuous work at high-

temperature conditions, gas cooling and spray cooling are used for the infrared temperature sensor and rolls, respectively.

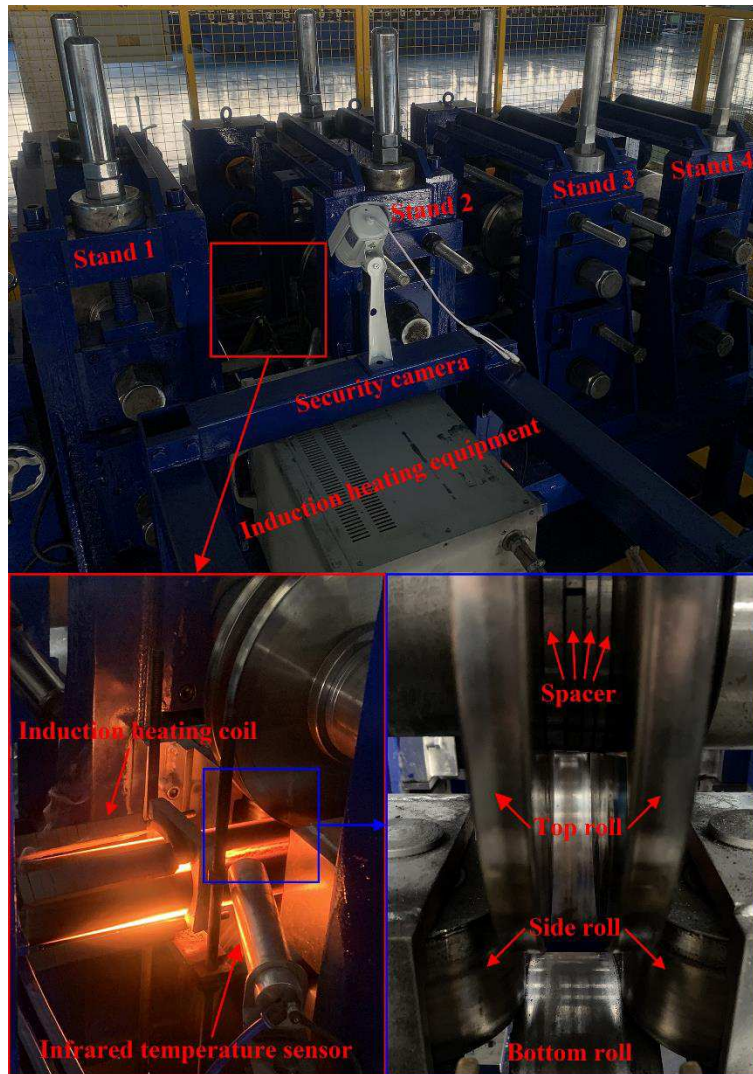


**Fig. 4** Experimental setup of HRF line

### 3.3 Measurement of the responses

The three responses investigated in this study are yield strength, outer corner radius, and microcrack length. After the square tube is hot roll-formed under each combination of process parameters, the tensile samples and metallographic specimens of the corner section will be sampled in the middle of the square tube. Considering that both ends of the tensile samples are not

panels or round bars, the special V-shaped clamp is designed and made for the tensile tests, as shown in Fig. 5. The length and width of the original gauge length of the tensile samples are 30 mm and 12.5 mm, respectively. The tensile tests are carried out on an electrical universal material testing machine with a tensile rate of  $1 \text{ mm} \cdot \text{min}^{-1}$  and the values of yield strength  $S_y$  are recorded.

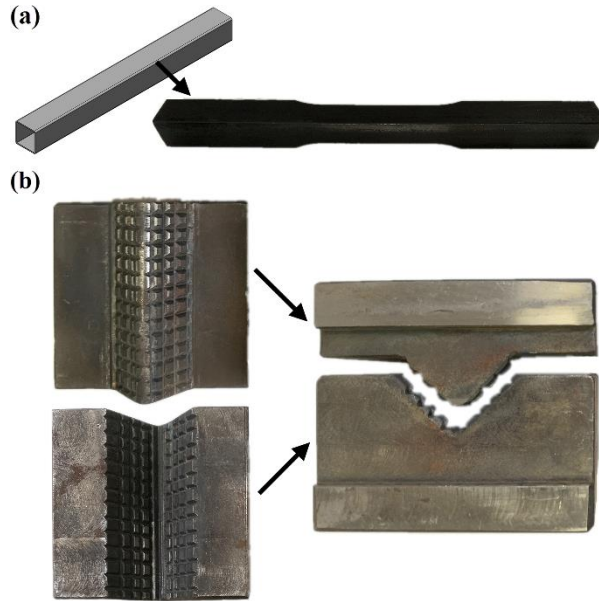


**Fig. 5** Tensile sample (a) and V-shaped clamp (b)

The metallographic specimens are inlaid, grounded, polished, and then observed under an optical microscope. The definition of outer corner radius  $R_o$  and microcrack length  $L_c$  for different specimens is shown in Fig. 6. The outer corner radius  $R_o$  is defined as the radius of the arc determined by points  $E$ ,  $F$ , and  $G$ , while the microcrack length  $L_c$  is defined as the vertical distance from the germination location to the deepest location of the microcrack. Point  $F$  is the middle point of the outer corner while points  $E$  and  $G$  are the points of tangency of the straight section to the outer corner for the cold and hot composite roll-formed square tube. As can be seen from Fig.6, the minimum value of  $L_c$  is 0 when there is no microcrack and the two-dimensional morphology of the microcrack is sometimes discontinuous. The width of the microcrack is beyond the scope

of the results discussed in this paper. To reduce measurement error, each response of the specimens is measured three times and the averaged value is recorded.

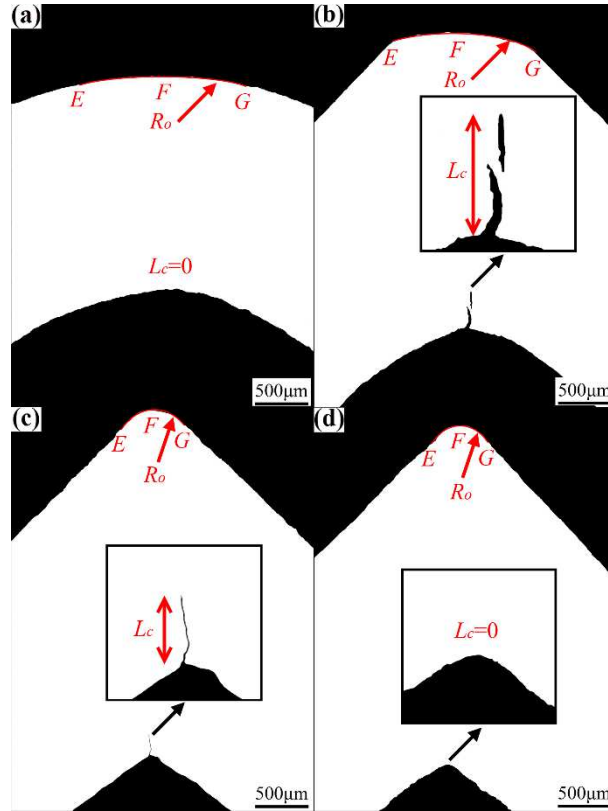


**Fig. 6** Definition of  $R_o$  and  $L_c$ : (a) cold roll-formed square tube; (b), (c), and (d) cold and hot composite roll-formed square tube

## 4 Results and discussion

### 4.1 Experimental results

To examine the comprehensive relationships of the three design variables (heating power, line velocity, and deformation amount) to the three responses (yield strength, outer corner radius, and microcrack length) by RSM, 15 experiments according to the BBD are performed randomly and presented in Table 3. The yield strength values are rounded to integers, while the values of the other two responses are rounded to two significant digits after the decimal point.

**Table 3.** Box-Behnken design for the three design variables and three responses

No.	Linear velocity $V/ (\text{m}\cdot\text{min}^{-1})$	Heating power $P/ (\text{kW})$	Deformation amount $A/ (\text{mm})$	Yield strength $S_y/ (\text{MPa})$	Outer corner radius $R_o/ (\text{mm})$	Microcrack length $L_c/ (\text{mm})$
1	4	47.5	5	957	1.96	0.84
2	4	52.5	4	943	2.17	0.51
3	3	47.5	4	930	1.87	0.38
4	3	52.5	3	881	2.27	0.080
5	2	52.5	4	766	0.32	0
6	3	42.5	5	966	2.030	0.85
7	3	52.5	5	890	0.72	0.21
8	2	42.5	4	913	1.81	0.34
9	3	47.5	4	932	1.88	0.40
10	4	47.5	3	950	2.39	0.50
11	3	42.5	3	962	2.56	0.49
12	2	47.5	5	867	0.40	0.18
13	3	47.5	4	925	1.96	0.37
14	4	42.5	4	971	2.41	1.02
15	2	47.5	3	856	2.080	0

#### 4.2 Model fitting and statistical analysis for the responses

The quadratic mathematical models to describe the relations between the responses and the design variables can be expressed as Eq. (7) ~ (9):

$$y_1 = 929 + 52.37x_1 - 41.5x_2 + 3.88x_3 + 29.75x_1x_2 - x_1x_3 + 1.25x_2x_3 - 24x_1^2 - 6.75x_2^2 + 2.5x_3^2 \quad (7)$$

$$y_2 = 1.9 + 0.54x_1 - 0.4163x_2 - 0.5238x_3 + 0.3125x_1x_2 + 0.3125x_1x_3 - 0.255x_2x_3 - 0.2067x_1^2 - 0.0192x_2^2 + 0.0108x_3^2 \quad (8)$$

$$y_3 = 0.3833 + 0.2937x_1 - 0.2375x_2 + 0.1263x_3 - 0.0425x_1x_2 + 0.04x_1x_3 - 0.0575x_2x_3 + 0.0283x_1^2 + 0.0558x_2^2 - 0.0317x_3^2 \quad (9)$$

where  $x_1$ ,  $x_2$ , and  $x_3$  are the coded values of linear velocity, heating power, and deformation amount, respectively,  $y_1$ ,  $y_2$ , and  $y_3$  are the actual values of yield strength, outer corner radius, and microcrack length, respectively.

Fig. 7 shows the comparison between the actual and predicted values of yield strength, outer corner radius, and microcrack length. It indicates that the mathematical models agree well with the actual situation because the data points tend to be close to the diagonal line, which means the residuals are very small.

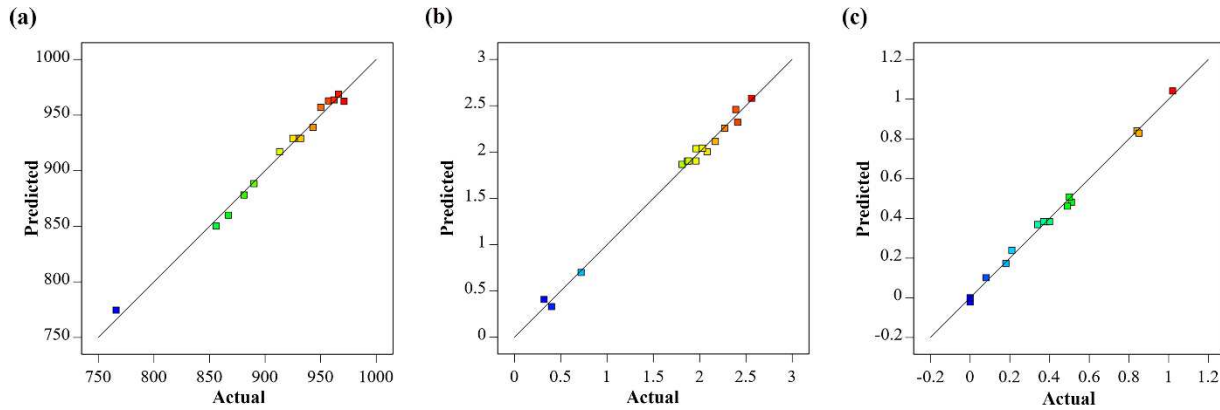


**Fig. 7** Comparison diagram of the actual and predicted values: (a) yield strength; (b) outer corner radius; (c) microcrack length

The analysis of variance (ANOVA) is carried out to estimate the validity of the mathematical model and the effect of every model term on the response. The P-value is used to check the significance, which means the response is greatly determined by the model term whose

P-value is sufficiently low (less than or equal to the significance level of 0.05). On the contrary, the higher the F-value, the stronger the significance of the model item.

The ANOVA of the mathematical model for the yield strength is shown in Table 4. All decimals greater than 0.0001 are rounded to two significant digits after the decimal point. The F-value (58.68) and P-value (0.00016) imply the model is significant, while the F-value (9.46) and P-value (0.097) imply the lack of fit is not significant. If the lack of fit is significant, the higher-order model terms should be taken into consideration to improve the accuracy of the model. According to the F-value and P-value, there are four significant model terms, among which the linear velocity  $x_1$  and heating power  $x_2$  have the greatest influence, followed by the quadratic effect of the linear velocity  $x_1^2$  and the linear-by-linear interaction effect between the linear velocity  $x_1$  and heating power  $x_2$ . The deformation amount  $x_3$  and other model terms containing it seem to have little influence on the yield strength.

**Table 4.** Analysis of variance for the mathematical model of yield strength

Source	Sum of Squares	df	Mean Square	F-value	P-value	
Model	41692.18	9	4632.46	58.68	0.00016	significant
$x_1$	21945.13	1	21945.13	277.96	<0.0001	significant
$x_2$	13778.00	1	13778.00	174.52	<0.0001	significant
$x_3$	120.12	1	120.12	1.52	0.27	
$x_1x_2$	3540.25	1	3540.25	44.84	0.0011	significant
$x_1x_3$	4.00	1	4.00	0.051	0.83	
$x_2x_3$	6.25	1	6.25	0.079	0.79	

$x_1^2$	2126.77	1	2126.77	26.94	0.0035	significant
$x_2^2$	168.23	1	168.23	2.13	0.20	
$x_3^2$	23.077	1	23.077	0.29	0.61	
Residual	394.75	5	78.95			
Lack of Fit	368.75	3	122.92	9.46	0.097	
Pure Error	26	2	13			
Cor Total	42086.93	14				

The ANOVA of the mathematical model for the outer corner radius is shown in Table 5. The F-value and P-value of the lack of fit are 6.065 and 0.14, respectively while the F-value and P-value of the model are 80.44 and less than 0.0001, respectively, which indicates the model is significant enough and no higher-order model terms need to be considered. The linear velocity and deformation amount have the greatest influence on the outer corner radius, followed by the heating power. In addition, all the linear-by-linear interaction effects, and the quadratic effect of the linear velocity  $x_1^2$  are also significant.

**Table 5.** Analysis of variance for the mathematical model of outer corner radius

Source	Sum of Squares	df	Mean Square	F-value	P-value	
Model	7.12	9	0.79	80.44	<0.0001	significant
$x_1$	2.33	1	2.33	237.35	<0.0001	significant
$x_2$	1.39	1	1.39	141.032	<0.0001	significant
$x_3$	2.19	1	2.19	223.28	<0.0001	significant

$x_1x_2$	0.39	1	0.39	39.74	0.0015	significant
$x_1x_3$	0.39	1	0.39	39.74	0.0015	significant
$x_2x_3$	0.26	1	0.26	26.46	0.0036	significant
$x_1^2$	0.16	1	0.16	16.046	0.010	significant
$x_2^2$	0.0014	1	0.0014	0.14	0.73	
$x_3^2$	0.00043	1	0.00043	0.044	0.84	
Residual	0.049	5	0.0098			
Lack of Fit	0.044	3	0.015	6.065	0.14	
Pure Error	0.0049	2	0.0024			
Cor Total	7.16	14				

---

The ANOVA of the mathematical model for microcrack length is shown in Table 6. As can be seen from the table, the model is significant with a large F-value (128.34) and an extremely small P-value ( $<0.0001$ ), while the lack of fit is still not significant with a smaller F-value (7.46) and larger P-value (0.12). The linear velocity  $x_1$  has the most significant influence on the microcrack length with the largest F-value (606.42), followed by the heating power  $x_2$  and deformation amount  $x_3$ . Besides, the linear-by-linear interaction effect between the heating power  $x_2$  and deformation amount  $x_3$ , and the quadratic effect of the heating power  $x_2^2$  also significantly influence the microcrack length.

**Table 6.** Analysis of variance for the mathematical model of microcrack length

Source	Sum of Squares	df	Mean Square	F-value	P-value	
Model	1.31	9	0.15	128.34	<0.0001	significant
$x_1$	0.69	1	0.69	606.42	<0.0001	significant
$x_2$	0.45	1	0.45	396.41	<0.0001	significant
$x_3$	0.13	1	0.13	112.017	0.00013	significant
$x_1x_2$	0.0072	1	0.0072	6.35	0.053	
$x_1x_3$	0.0064	1	0.0064	5.62	0.064	
$x_2x_3$	0.013	1	0.013	11.62	0.019	significant
$x_1^2$	0.0030	1	0.0030	2.60	0.17	
$x_2^2$	0.012	1	0.012	10.11	0.025	significant
$x_3^2$	0.0037	1	0.0037	3.25	0.13	
Residual	0.0057	5	0.0011			
Lack of Fit	0.0052	3	0.0017	7.46	0.12	
Pure Error	0.00047	2	0.00023			
Cor Total	1.32	14				

### 4.3 Interaction effects of the design variables on the yield strength

The response surfaces (3D) are plotted to investigate the interaction effects of the design variables on the yield strength (Fig. 8). Although the 3D surfaces can reveal the response distribution when the coded values of two design variables change within [-1,1] and the coded

value of the third one is fixed, the interaction effects between the two design variables on the response are not clear enough. Therefore, Fig. 9 is drawn to show the interaction effects more visually while the coded values of the two design variables are fixed.

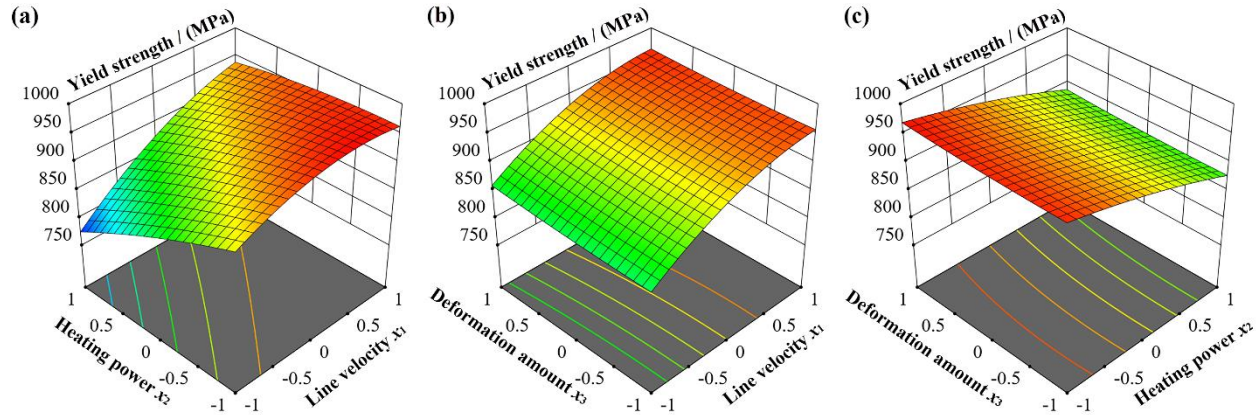


**Fig. 8** Response surfaces (3D) showing the interaction effects of the linear velocity  $x_1$ , heating power  $x_2$ , and deformation amount  $x_3$  on the yield strength: (a) deformation amount  $x_3 = 0$ ; (b) heating power  $x_2 = 0$ ; (c) linear velocity  $x_1 = 0$

As can be seen from Fig.9, the increase in linear velocity and deformation amount, as well as the decrease in heating power will lead to an increase in yield strength. The yield strength in Fig.9a ~ d varies greatly compared to Fig.9e ~ f, indicating that the linear velocity and heating power are more significant than the deformation amount. The non-parallel distribution of the two lines can be observed in Fig.9a and Fig.9c, which indicates that the interaction effect between the linear velocity and heating power is significant. The result of significant model terms agrees well with the ANOVA.

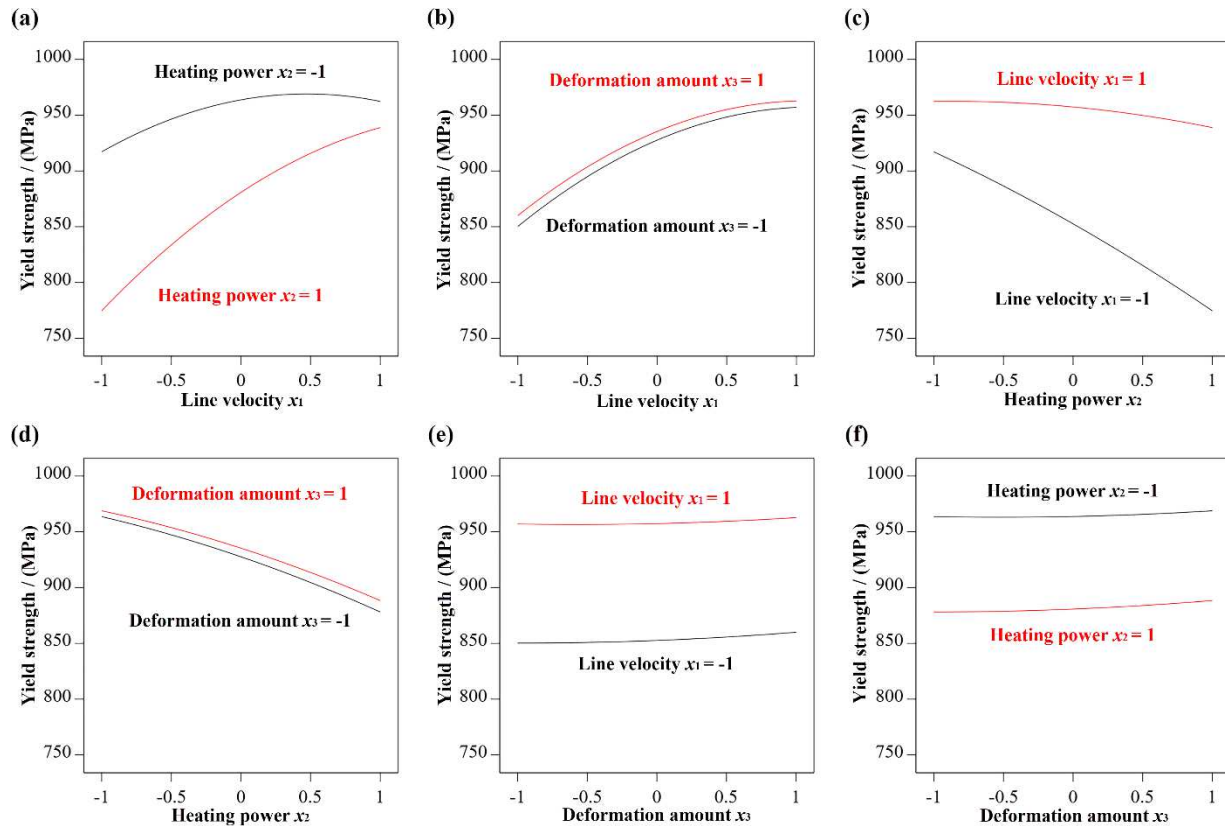


**Fig. 9** Interaction effects of the linear velocity  $x_1$ , heating power  $x_2$ , and deformation amount  $x_3$  on the yield strength: (a), (c) deformation amount  $x_3 = 0$ ; (b), (e) heating power  $x_2 = 0$ ; (d), (f) linear velocity  $x_1 = 0$

For the corner section made of QSTE700TM AHSS, the strengthening mechanism is mainly fine grain strengthening, followed by deformation strengthening, which means that finer grain size and higher dislocation density are beneficial to the improvement of yield strength. With the increase in heating power and the decrease in linear velocity, the heating temperature in the corner section will increase greatly and the grain will grow up more easily before HRF, which can explain the rapid decline of yield strength when the line velocity  $x_1$  is -1 or the heating power  $x_2$  is 1 in Fig.9a and Fig.9c, as well as the lower value level in Fig9e ~ f. On the other hand, increasing the heating temperature is also beneficial to the dynamic recrystallization

softening process to counteract the deformation strengthening process, while increasing the deformation amount is beneficial to both processes. This is the main reason why the effect of deformation amount is slight in Fig.9e ~ f.

#### 4.4 Interaction effects of the design variables on the outer corner radius

Fig. 10 is the response surfaces (3D) to represent the interaction effects of the design variables on the outer corner radius. Fig. 10a is very similar to Fig. 10b, while the ANOVA result in Table 5 and polynomial coefficient in Eq. (8), of the model terms  $x_1x_2$  and  $x_1x_3$  are the same accordingly.

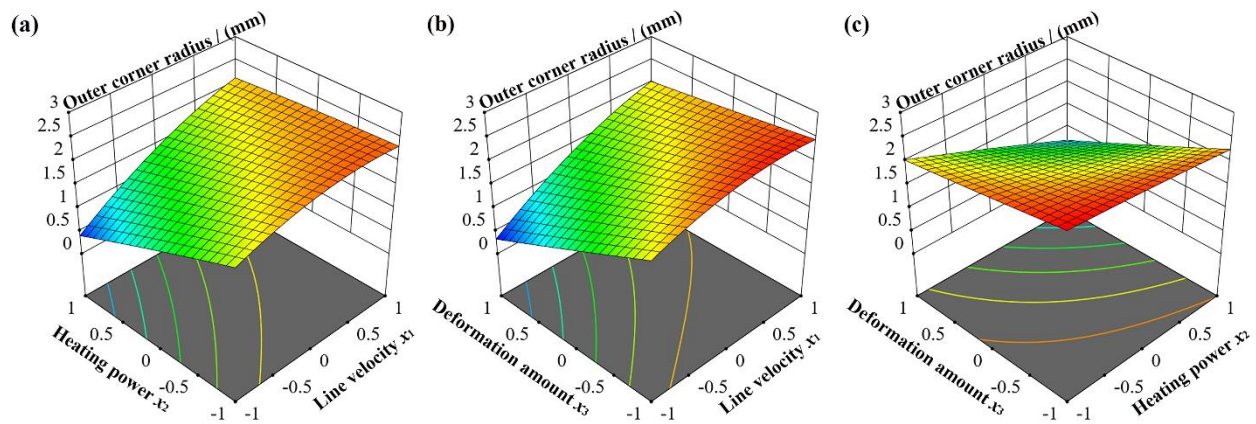


**Fig. 10** Response surfaces (3D) showing the interaction effects of the linear velocity  $x_1$ , heating power  $x_2$ , and deformation amount  $x_3$  on the outer corner radius: (a) deformation amount  $x_3 = 0$ ; (b) heating power  $x_2 = 0$ ; (c) linear velocity  $x_1 = 0$

From the interaction effects diagram shown in Fig.11, it is found that the increase in heating power and deformation amount, and the decrease in linear velocity will result in a decrease in the outer corner radius. The dramatic changes in the outer corner radius and non-parallel distribution of the two lines can be observed in Fig.11a ~ f, which indicates that all the

design variables and interaction effects are significant, matching the result of ANOVA in Table 5.

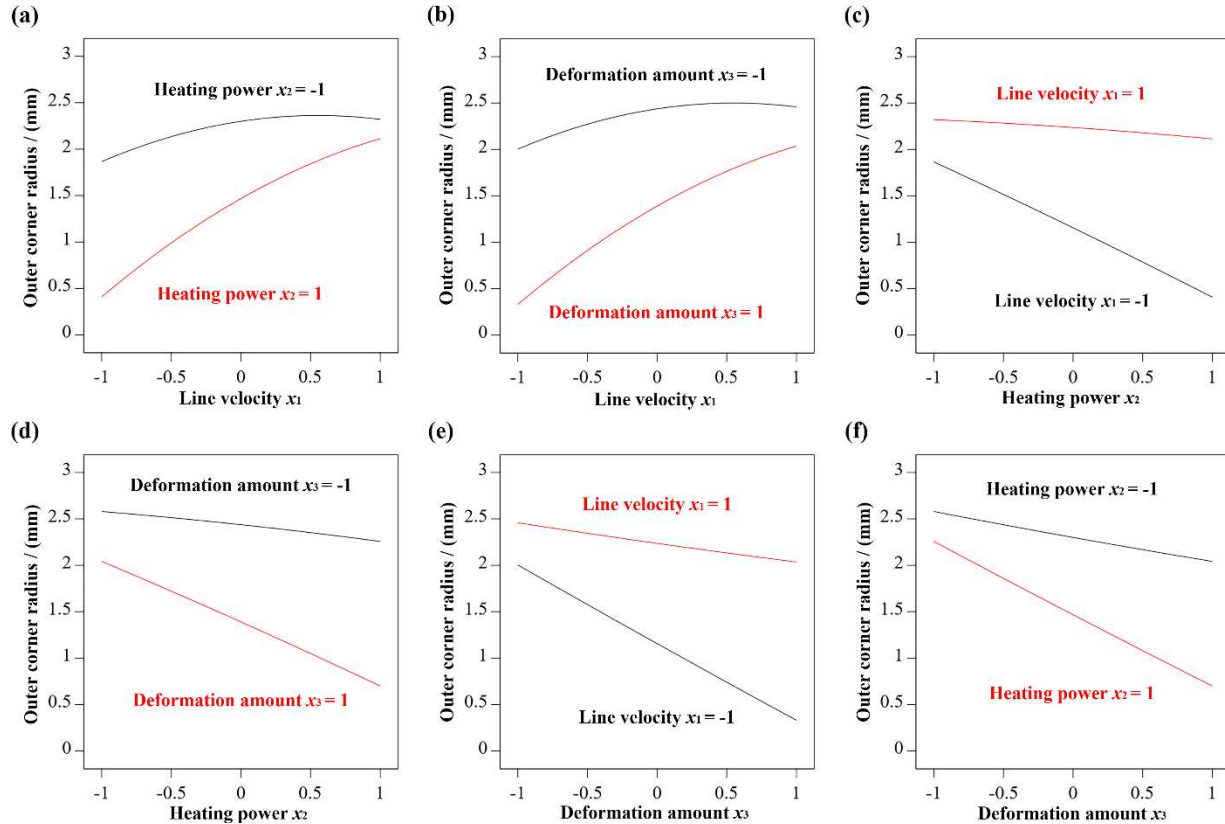


**Fig. 11** Interaction effects of the linear velocity  $x_1$ , heating power  $x_2$ , and deformation amount  $x_3$  on the outer corner radius: (a), (c) deformation amount  $x_3 = 0$ ; (b), (e) heating power  $x_2 = 0$ ; (d), (f) linear velocity  $x_1 = 0$

As mentioned earlier, one of the main objectives of HRF is to reduce the outer corner radius for easier assembly and welding. Moreover, the reduction of the outer corner radius is essentially the metal accumulation in the corner section. As can be seen from Fig.11 a ~ d, with the increase in heating power and the decrease in line velocity, the heating temperature and ductility of the AHSS will also increase, which brings a decrease in the outer corner radius. On

the other hand, a greater deformation amount will drive more metal to flow to the corner section, so the outer corner radius will also decrease (Fig.11e ~ f). In conclusion, high heating temperature and large deformation amount are two necessary conditions for obtaining a small outer corner radius, which can explain why it is difficult to reduce the outer corner radius to less than 2 mm when the line velocity  $x_1$  is 1, the heating power  $x_2$  is -1, or the deformation amount  $x_3$  is -1.

#### 4.5 Interaction effects of the design variables on the microcrack length

In Fig. 12, the 3D response surfaces are developed for the microcrack length with two varying design variables, while the coded value of the third one is fixed at 0. A small number of microcrack length values are negative, contrary to the actual situation, which can be considered 0.

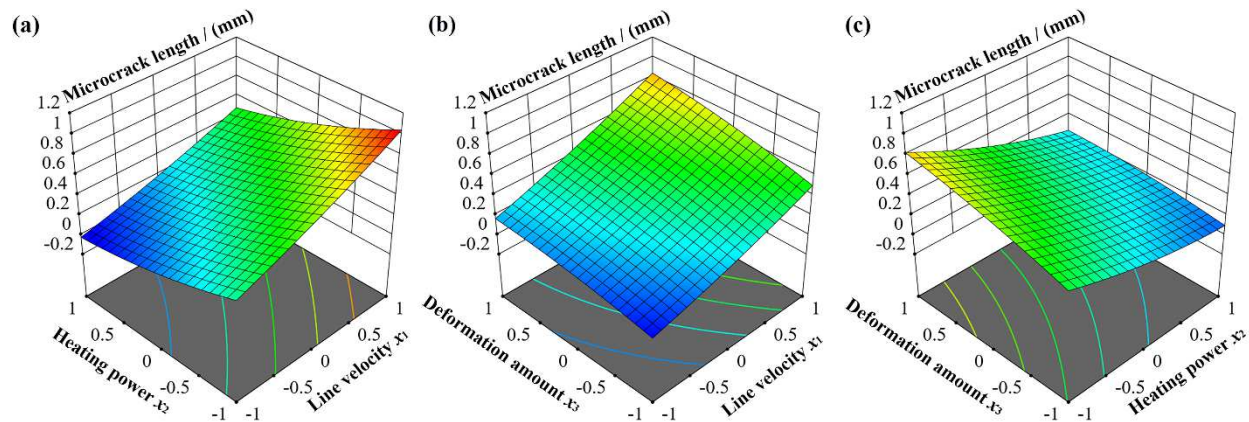


**Fig. 12** Response surfaces (3D) showing the interaction effects of the linear velocity  $x_1$ , heating power  $x_2$ , and deformation amount  $x_3$  on the microcrack length: (a) deformation amount  $x_3 = 0$ ; (b) heating power  $x_2 = 0$ ; (c) linear velocity  $x_1 = 0$

Fig.13 illustrates the interaction effects of the three design variables on the microcrack length. It can be noted that the microcrack length will increase as the linear velocity and

deformation amount increase, as well as the heating power decreases. According to the variation range of the microcrack length, the design variable with the most significant influence is the linear velocity, followed by the heating power, and deformation amount. There is an obvious non-parallel feature for the two lines in Fig13d and Fig13f, which indicates that the interaction effect between the heating power and deformation amount is significant. The significance of the design variables is consistent with the ANOVA in Table 6.

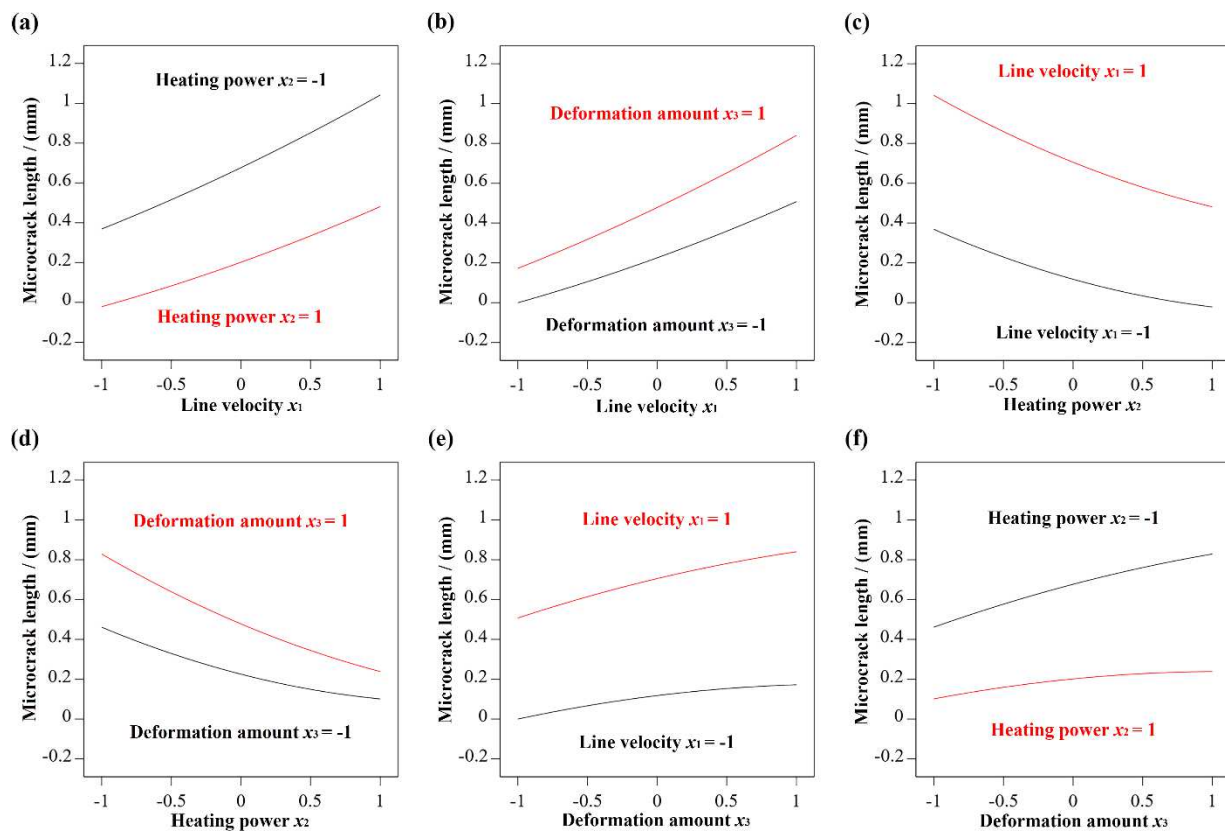


**Fig. 13** Interaction effects of the linear velocity  $x_1$ , heating power  $x_2$ , and deformation amount  $x_3$  on the microcrack length: (a), (c) deformation amount  $x_3 = 0$ ; (b), (e) heating power  $x_2 = 0$ ; (d), (f) linear velocity  $x_1 = 0$

During the HRF, the immediate cause of microcrack defect is that the compressive stress of the corner section exceeds the strength limit of AHSS, while the root cause is the insufficient

ductility caused by lower heating temperature, and excessive deformation amount. The linear velocity is the most significant design variable for the microcrack length. Since the heating time increases as the linear velocity decreases, the microcrack length will significantly decrease (Fig.13a ~ b). On the other hand, due to the skin effect of the induction heating technology, the temperature of the inner corner section rises more slowly than that of the outer corner section during the heating process. Thus, a longer heating time is beneficial to uniformly heat the corner section along the thickness direction, which is very important for improving the microcrack defect. Although the heating power, as shown in Fig.13c ~ d, has less influence on the microcrack length than the linear velocity, its increase can still significantly reduce the microcrack length. The range of microcrack length is small in Fig.13e ~ f, but there is a large difference between high and low levels, indicating that the deformation amount has the lowest significance on the microcrack length, because the ductility of AHSS plays a more decisive role in the generation and development of microcrack defect.

## **5 Optimization and verification**

### **5.1 Multi-response optimization**

The discussions above have been focused on the interaction effects of linear velocity, heating power, and deformation amount on the three responses. In this section, a multi-response optimization process is presented to obtain the combination of process parameters that can meet the target values of all three responses.

As stated above, the yield strength of QSTE700TM AHSS is more than 700 MPa. However, due to deformation strengthening, the square tube corner section's yield strength is expected to increase by about 10 % to 20 %, which means the target value of the yield strength is between 770

MPa and 840 MPa. The optimal theoretical value of the outer corner radius is 0. However, it is not easy to achieve this theoretical value in the actual situation, so the target value of the outer corner radius is set as 10% of the wall thickness, which means the target value of the outer corner radius is 0.2 mm. The target value of the microcrack length is undoubtedly 0 because the existence of the microcrack means that the square tube is not qualified. Thus, the constrained condition of yield strength  $y_1$ , as well as the objective functions of outer corner radius  $y_2$  and microcrack length  $y_3$  can be expressed as Eq. (10).

$$770 \leq y_1 \leq 840, \quad y_2 = 0.2, \quad y_3 = 0 \quad (10)$$

Table 7 shows ten groups of process parameters combinations and the corresponding predicted values of responses. All the values are rounded to three significant digits after the decimal point while the scientific counting method is used for the microcrack length. It is found that no matter the process parameters or responses, the difference between the values of the ten groups is very small. Considering the actual situation, the optimal linear velocity, heating power, and deformation amount are  $2 \text{ m} \cdot \text{min}^{-1}$ , 51.8 kW, and 4.3 mm, respectively.

**Table 7.** Optimization results

No.	Linear velocity $V/(\text{m}\cdot\text{min}^{-1})$	Heating power $P/(\text{kW})$	Deformation amount $A/(\text{mm})$	Yield strength $S_y/(\text{MPa})$	Outer corner radius $R_o/(\text{mm})$	Microcrack length $L_c/(\text{mm})$
1	2.0369	52.128	4.294	787.557	0.200	1.960e-07
2	2.0723	52.472	4.285	786.303	0.200	2.785e-07
3	2.0234	52.00204	4.297	787.959	0.200	1.0526e-06
4	2.0534	52.286	4.290	787.00968	0.200	1.441e-06
5	2.0153	51.928	4.299	788.182	0.200	1.100e-06
6	2.0751	52.500	4.284	786.191	0.200	1.258e-06
7	2.0472	52.227	4.292	787.223	0.200	1.450e-06
8	2.0409	52.166	4.293	787.432	0.200	5.990e-07
9	2.00706	51.852	4.301	788.397	0.200	8.145e-07
10	2.0300	52.063	4.296	787.769	0.200	1.0743e-06

## 5.2 Experimental verification

Experimental verification with the optimal combination of process parameters is carried out to validate the adequacy of the optimization. The results of CRF and CHCRF are shown in Table 8. Under the optimal process parameter combination, the yield strength and outer corner radius of the cold and hot composite roll-formed AHSS square are 804 and 0.23, respectively, which are very close to the target value of 788 and 0.2, while the microcrack length is completely

consistent with the target value 0. Since the error is the ratio of the absolute difference value between the predicted and actual values to the actual value, the error values of the yield strength, outer corner radius, and microcrack length are about 2 %, 13 %, and 0 %, respectively. The average error of the three responses is about 5 %, indicating that the optimization design has good prediction accuracy.

**Table 8.** Comparison of the results for two forming processes

Responses	CRF	CHCRF		
	Actual value	Predicted value	Actual value	Error
Yield strength $S_y$ / (MPa)	882	788	804	2 %
Outer corner radius $R_o$ / (mm)	3.67	0.20	0.23	13 %
Microcrack length $L_c$ / (mm)	0	0	0	0 %
Corner thickness $T_c$ / (mm)	1.97	N/A	3.15	N/A

Compared to the cold roll-formed square tube, although the yield strength of cold and hot composite roll-formed square tube decreased slightly by about 9 %, it still exceeds the yield strength of QSTE700TM by about 15%. On the other hand, the outer corner radius is about 12 % of the wall thickness, which is successfully reduced by about 94 %. Due to the reasonable optimization of the process parameters, no microcracks are produced during the HRF. Table 8 shows that the corner thickness is increased by about 60 % after the HRF, which reaches 1.6 times the wall thickness of 2 mm. The cross-section comparison between the cold and hot composite roll-formed AHSS square tube (right) and the traditional cold roll-formed AHSS square tube (left) is shown in Fig. 14.

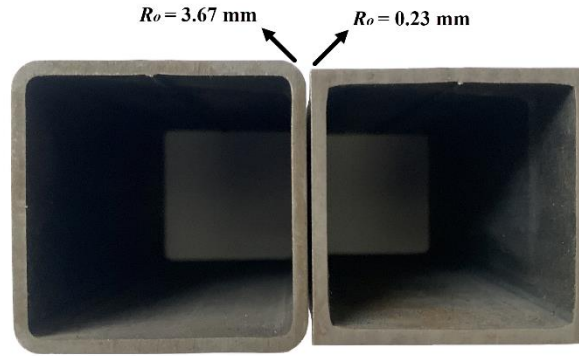


**Fig. 14** Cross-section comparison of the tubes

## 6 Conclusions and future work

Based on the response surface methodology with Box–Behnken design, this paper presents a study on the optimization design of process parameters for cold and hot composite roll forming of AHSS square tube. The quadratic mathematical model is developed to express the relationship between the three process parameters (heating power, line velocity, and deformation amount) and yield strength, outer corner radius, and microcrack length of the AHSS square tube corner section respectively. The optimization design of process parameters is presented according to the evaluation criteria and the experimental verification is carried out under the optimal combination of the process parameters. From this study, the main conclusions can be made as follows:

(1) The yield strength is mainly determined by the linear velocity, followed by the heating power because these two process parameters have a decisive influence on the heating temperature. The strength decreases with the increase in heating temperature, while the deformation amount has little impact on the yield strength.

(2) The outer corner radius is influenced significantly by all the three process parameters as the ductility improvement caused by a higher heating temperature is the precondition while a larger deformation amount provides driving force to decrease the outer corner radius.

(3) Similar to the outer corner radius, all three parameters have a significant influence on the microcrack length, but on the contrary, a larger deformation is conducive to the occurrence of the microcrack. The linear velocity plays a major role because a slower velocity is beneficial to the heat conduction in the inner corner to improve the ductility, where the microcracks germinate.

(4) The AHSS square tube with a corner thickness of 3.15 mm, an outer corner radius of 0.23 mm, and a corner yield strength of 804 MPa, without microcrack defect, is obtained using the optimal process parameter combination. The average error between the predicted and the actual values of the three responses is about 5 %, indicating the high reliability of the optimization design.

The AHSS square tube with sharp thickened corners formed by CHCRF breaks through the limitation of large corner radius, thickness reduction, and microcrack defect of cold roll-formed products, which fills the market gap and shows broad application prospects. CHCRF provides fresh ideas for scholars and engineers engaged in the CRF field to research and develop new manufacturing technologies. As CHCRF is an emerging technology, future research will focus on the application of the technology to more steel tubes with different strength grades, shape sizes, and thicknesses, which will bring new challenges to both the process parameters and equipment.

## **7 Declarations**

### **Ethical Approval**

Not applicable

### **Consent to Participate**

Not applicable

### **Consent to Publish**

Not applicable

## Authors Contributions

Jingtao Han provided the ideas, funding, and supervision. Yu Wang designed and performed the experiments with Junyuan Wu. Yu Wang analyzed the results and wrote the manuscript. Zelalem Abathun Mehari contributed to the review and editing of the manuscript. All authors read and approved the final manuscript.

## Funding

Not applicable

## Competing interest

The authors declare that they have no competing interests.

## Availability of data and materials

Not applicable

## References

1. Zhang Y, Lai X, Zhu P, Wang W (2006) Lightweight design of automobile component using high strength steel based on dent resistance. *Mater Des* 27:64–68. <https://doi.org/10.1016/j.matdes.2004.09.010>
2. Song H, Yoo J, Kim S-H, et al (2017) Novel ultra-high-strength Cu-containing medium-Mn duplex lightweight steels. *Acta Mater* 135:215–225. <https://doi.org/10.1016/j.actamat.2017.06.035>
3. Khalkhali A, Miandoabchi E (2020) The application of equivalent modeling of joints for bending simulation of hybrid aluminum/high strength steel thin-walled sections joined by clinching. *Thin-Walled Struct* 157:107089. <https://doi.org/10.1016/j.tws.2020.107089>
4. Bhattacharyya D, Smith PD, Yee CH, Collins IF (1984) The prediction of deformation length in cold roll-forming. *J Mech Work Technol* 9:181–191. [https://doi.org/10.1016/0378-3804\(84\)90004-4](https://doi.org/10.1016/0378-3804(84)90004-4)
5. Yuan C, Li S, Huang J, et al (2021) Effect of hierarchical martensitic microstructure on fatigue crack growth behavior of ultra-high strength hot stamping steel. *Mater Charact* 174:111041. <https://doi.org/10.1016/j.matchar.2021.111041>
6. Cha W, Kim N (2014) Quantification of micro-cracks on the bending surface of roll formed products using the GTN model. *Met Mater Int* 20:841–850. <https://doi.org/10.1007/s12540-014-5008-8>

7. Chen P, Koç M (2007) Simulation of springback variation in forming of advanced high strength steels. *J Mater Process Technol* 190:189–198. <https://doi.org/10.1016/j.jmatprotec.2007.02.046>
8. Choi HS, Yoon JW, Lee JS, Kim GH (2019) A Springback Prediction of 1.5 GPa Grade Steel in Roll Forming Process for Automotive Sill-Side Inner Component. *Key Eng Mater* 794:267–274. <https://doi.org/10.4028/www.scientific.net/KEM.794.267>
9. Liu X, Cao J, Chai X, et al (2018) Experimental and numerical prediction of the local thickness reduction defect of complex cross-sectional steel in cold roll forming. *Int J Adv Manuf Technol* 95:1837–1848. <https://doi.org/10.1007/s00170-017-1279-9>
10. Arola AM, Kesti V, Ruoppa R (2015) The Effect of Punch Radius on the Deformation of Ultra-High Strength Steel in Bending. *Key Eng Mater* 639:139–146. <https://doi.org/10.4028/www.scientific.net/KEM.639.139>
11. Vorkov V, García AT, Duflou JR (2020) Bending Parameters in Heat Assisted Air Bending of High Strength Steels. *Procedia Manuf* 47:1314–1318. <https://doi.org/10.1016/j.promfg.2020.04.250>
12. Abathun MZ, Han J, Yu W (2021) Effects of manufacturing methods and production routes on residual stresses of rectangular and square hollow steel sections: a review. *Arch Civ Mech Eng* 21:100. <https://doi.org/10.1007/s43452-021-00193-8>
13. Sun Y, Luzin V, Duan Y, et al (2020) Forming-Induced Residual Stress and Material Properties of Roll-Formed High-Strength Steels. *Automot Innov* 3:210–220. <https://doi.org/10.1007/s42154-020-00112-2>
14. Lindgren M (2007) Experimental investigations of the roll load and roll torque when high strength steel is roll formed. *J Mater Process Technol* 191:44–47. <https://doi.org/10.1016/j.jmatprotec.2007.03.041>
15. Moneke M, Groche P (2021) The origin of end flare in roll formed profiles. *Int J Mater Form* 14:1439–1461. <https://doi.org/10.1007/s12289-021-01640-w>
16. Moneke M, Groche P (2021) Control of residual stresses in roll forming through targeted adaptation of the roll gap. *J Mater Process Technol* 294:117129. <https://doi.org/10.1016/j.jmatprotec.2021.117129>
17. Jiao-Jiao C, Jian-Guo C, Qiu-Fang Z, et al (2020) A novel approach to springback control of high-strength steel in cold roll forming. *Int J Adv Manuf Technol* 107:1793–1804. <https://doi.org/10.1007/s00170-020-05154-8>
18. Su C, Liu J, Zhao Z, et al (2020) Research on roll forming process and springback based on five-boundary condition forming angle distribution function. *J Mech Sci Technol* 34:5193–5204. <https://doi.org/10.1007/s12206-020-1121-4>
19. Abeyrathna B, Rolfe B, Hodgson P, Weiss M (2016) A first step towards a simple in-line shape compensation routine for the roll forming of high strength steel. *Int J Mater Form* 9:423–434. <https://doi.org/10.1007/s12289-015-1238-7>
20. Tajik Y, Moslemi Naeini H, Azizi Tafti R, Shirani Bidabadi B (2018) A strategy to reduce the twist defect in roll-formed asymmetrical-channel sections. *Thin-Walled Struct* 130:395–404. <https://doi.org/10.1016/j.tws.2018.05.013>
21. Shirani Bidabadi B, Moslemi Naeini H, Salmani Tehrani M, Barghikar H (2016) Experimental and numerical study of bowing defects in cold roll-formed, U-channel sections. *J Constr Steel Res* 118:243–253. <https://doi.org/10.1016/j.jcsr.2015.11.007>

22. Groche P, Zettler A, Berner S, Schneider G (2011) Development and verification of a one-step-model for the design of flexible roll formed parts. *Int J Mater Form* 4:371–377. <https://doi.org/10.1007/s12289-010-0998-3>
23. Yan Y, Wang H, Li Q, Guan Y (2016) Finite element simulation of flexible roll forming with supplemented material data and the experimental verification. *Chin J Mech Eng* 29:342–350. <https://doi.org/10.3901/CJME.2015.0824.106>
24. Park J-C, Yang D-Y, Cha M, et al (2014) Investigation of a new incremental counter forming in flexible roll forming to manufacture accurate profiles with variable cross-sections. *Int J Mach Tools Manuf* 86:68–80. <https://doi.org/10.1016/j.ijmachtools.2014.07.001>
25. Ding S, Meehan PA, Daniel WJT (2011) A novel sheet metal forming method—Millipede forming. *J Mater Process Technol* 211:376–381. <https://doi.org/10.1016/j.jmatprotec.2010.10.012>
26. Sun Y, Li Y, Daniel WJT, et al (2017) Longitudinal strain development in Chain-die forming AHSS products: Analytical modelling, finite element analysis and experimental verification. *J Mater Process Technol* 243:322–334. <https://doi.org/10.1016/j.jmatprotec.2016.12.019>
27. Li Y, Sun Y, Xiao H, et al (2018) A numerical study on chain-die forming of the AHSS U-channel and contrast with roll forming. *Int J Mech Sci* 135:279–293. <https://doi.org/10.1016/j.ijmecsci.2017.11.034>
28. Lindgren M, Bexell U, Wikström L (2009) Roll forming of partially heated cold rolled stainless steel. *J Mater Process Technol* 209:3117–3124. <https://doi.org/10.1016/j.jmatprotec.2008.07.041>
29. Kim D-H, Darabi R, Jung D-W (2018) Investigation on the Effect of Pre-heating with Butane Gas Torch in Formability of High Tension Steel (HTS) by Using Taguchi Experimental Method in Roll Forming Process. *Trans Indian Inst Met* 71:1871–1884. <https://doi.org/10.1007/s12666-018-1319-7>
30. Peng XF, Chen Q, Wang Y, Liu J, Han JT, Yan PJ (2016) Effect of local induction heating on secondary roll-forming of high strength square tubes. *Chin J Eng* 38:973–978. <https://doi.org/10.13374/j.issn2095-9389.2016.07.012>
31. Li Q, Han F, Yang H (2016) Effect of forming processes on residual stresses and weld microstructure of roll-formed square tube. *J Iron Steel Res* 26:37-42. <https://doi.org/10.13228/j.boyuan.issn1001-0963.2014.01.006>
32. Bui QV, Ponthot JP (2008) Numerical simulation of cold roll-forming processes. *J Mater Process Technol* 202:275–282. <https://doi.org/10.1016/j.jmatprotec.2007.08.073>
33. Shirani Bidabadi B, Moslemi Naeini H, Azizi Tafti R, Mazdak S (2015) Experimental investigation of the ovality of holes on pre-notched channel products in the cold roll forming process. *J Mater Process Technol* 225:213–220. <https://doi.org/10.1016/j.jmatprotec.2015.06.008>
34. Kasaei MM, Moslemi Naeini H, Azizi Tafti R, Tehrani MS (2014) Prediction of maximum initial strip width in the cage roll forming process of ERW pipes using edge buckling criterion. *J Mater Process Technol* 214:190–199. <https://doi.org/10.1016/j.jmatprotec.2013.08.012>
35. Chen C, Shao Y, Tao Y, Wen H (2015) Optimization of dynamic microwave-assisted extraction of *Armillaria polysaccharides* using RSM, and their biological activity. *LWT - Food Sci Technol* 64:1263–1269. <https://doi.org/10.1016/j.lwt.2015.07.009>